Non-metal sensory electrode design and protocol of DNA-nucleobases in living cells exposed to oxidative stresses

M. Y. Emran,[1,2] S. A. El-Safty[1,*], M. M. Selim,[3] T. Minowa,[4] A. Elmarakbi,[5] M. A. Shenashen[1]

[1] Research Center for Functional Materials, National Institute for Materials Science, 1-2-1 Sengen, Tsukuba-shi, Ibaraki-ken 305-0047, Japan

[2] Chemistry Department, Faculty of Science, Al-Azhar University, Assiut 71524, Egypt

[3] Al-Aflaj College of Science and Human Studies, Prince Sattam Bin Abdulaziz University, Al-Aflaj, 710-11912, Saudi Arabia

[4] Nanotechnology Innovation Station, Materials, National Institute for Materials Science, 1-2-1 Sengen, Tsukuba 305-0047, Japan

[5] Faculty of Engineering and Environment, Northumbria University, Newcastle upon Tyne, NE1 8ST, UK

*Correspondence: sherif.elsafty@nims.go.jp

Homepage: https://samurai.nims.go.jp/profiles/sherif_elsafty

Abstract

Sensory protocols for evaluation of DNA distortion due to exposure to various harmful chemicals and environments in living cells are needed for research and clinical investigations. Here, a design of non-metal sensory (NMS) electrode was built by using boron-doped carbon spherules for detection of DNA nucleobases, namely, guanine (Gu), adenine (Ad), and thymine (Th) in living cells. The key-electrode based nanoscale NMS structures lead to voids with a facile diffusion, and strong binding events of the DNA nucleobases. Furthermore, the NMS geometric structures would significantly create electrode surfaces with numerous centrally active sites, curvature topographies, and anisotropic spherules. The NMS shows potential as sensitive protocol for DNA-nucleobases in living cells exposed to oxidative stresses. In one-step signaling assay, NMS shows high signaling transduction of Gu-, Ad-, and Th-DNA nucleobases targets with ultra-sensitive and low detection limits of 3.0, 0.36, and 0.34 nM, respectively, and a wide linear range of up to 1 µM. The NMS design and protocol show evidence of the role of surface construction features and B-atoms incorporated into the graphitic carbon network for creating abundant active sites with facile electron diffusion and heavily target loads along with within-/out-plane circular spheres. Indeed NMS, with spherule-rich interstitial surfaces can be used for sensitive and selective evaluation of damaged-DNA to various dysfunctional metabolism in the human body.

Keywords; Boron-doped carbon spherules; DNA-nucleobases; Thymine; Adenine; Guanine; Electrochemical sensor; Living cells; Oxidative stresses

1 Introduction

Deoxyribonucleic acid (DNA) and ribonucleic acid (RNA), which contain nitrogenous bases of guanine (Gu), adenine (Ad), thymine (Th), and cytosine, are dual-spiral biopolymer structures that are mainly responsible for the formation of human chromosomes [1, 2]. DNA functions can be determined according to the assignment of heritable information coding in living cells. DNA usually plays a key role in several biological interactions and in signaling and transducing energy across cells [2–4]. DNA damages are caused by multiple key conditions, such as lifestyle stress, exposure to ultraviolet (UV)/infrared (IR) irradiation, and utilization of carcinogenic chemicals and food preservatives [3-5]. Changes in DNA structures by binding, distortion or relocation, and denaturation would lead to aberrant biological activity [7, 8]. Therefore, sensitive monitoring and determination of DNA nucleobases are of particular interest to configure DNA-function and obtain high-quality human health. The concentration of DNA nucleobases in living cells could be used as an indicator of numerical diseases, such as AIDS, myocardial cellular energy status, and cancer [9, 10]. Developing sensor designs for sensitive and selective evaluation of damaged DNA in various dysfunctional metabolism disorders in the human body has gained much attention in bioscience and clinical diagnosis [1,2].

Ultra-trace detection, easy-to-use, fast response, and low-cost analysis techniques for DNA nucleobases are required for clinical monitoring and diagnosis. Therefore, various analytical techniques, such as gas chromatography [11], fluorescence [12], liquid chromatography [13], capillary electrophoresis [14], and electrochemical method [1, 2, 6, 7] have been used for screening of biomolecules. These analytical methods show evidence of sensitive determination of DNA nucleobases; however, electrochemical method is preferred for designing commercially effective analytical devices. Electrochemical techniques offer biomolecules sensing assays with high sensitivity, selectivity, and rapid response [15–20]. Fabrication of straightforward-to-use, inexpensive, and portable nano-scale sensors for detection of DNA nucleobases remains a challenge. Therefore, development of electrochemical nano-devices for detection of low levels of DNA nucleobases with high precision analytical technique is a challenge for clinical investigation.

Assays for simultaneous selective determination of Gu, Ad, and Th require highly active electrode surfaces that effectively show sensitive signaling and electron transfer kinetics at a low applied potential. Several approaches have reported to design electrochemical electrodes with highly stable signaling for sensitive and selective determination of Gu, Ad, and Th [2 ,4, 7, 21, 22]. Carbon-based structure geometrics [21, 23, 24], polymeric architects [4], and nanoparticles [22, 25–27], are widely used to fabricate electrodes through manipulation of advanced nanomaterials. Carbon-based materials are widely used to fabricate electrochemical sensor for Gu, Ad, and Th [28–33]. The key features of carbon electrodes for Gu, Ad, and Th are large surface coverage, porosity, surface heterogeneity with actively doped heteroatoms, such as P, N and B, and high electrical conductivity; these properties enable the synthesis of sensors with sensitive and selective binding capability to Gu, Ad, and Th [34–36]. In this regard, doping of heteroatoms is of interest. For instance, B dopants (i.e., p-type electron transfer) enhance electron transfer delocalization via the mechanistic formation of an ease +ve-hole vacancy on carbon electrode surfaces [37, 38]. Facile changes in the distribution of electronic clouds along the entire carbon networks (distortion of sp^2 graphitization) with B-dopants are apparent [39–41]. Therefore, the design of electrochemical nano-sensors based on B-doped carbon materials will create electrode surface pools with abundant central active sites, curvature surface topography, and anisotropic spherule geometrics for potential sensing assays of Gu, Ad, and Th in living cells.

Herein, we design non-metal sensory (NMS) electrode with B-doped carbon spherules for sensitive and selective signaling of Gu, Ad and Th DNA-nucleobases in living cells. NMS surfaces are fabricated with conjugated nano-spherules. The key structures of NMS enable to create electrodes with numerous centrally active sites, curvature surface topography, and anisotropic spherule geometrics. The fabrication of highly active and stable NMS electrodes leads to fast charge transport and sensitive and selective sensing assays of Gu-, Ad-, and Th-nucleobases in living cells (Scheme 1). NMS surfaces with a wide range of vacancies, including grooves, ridges irregular surface ripples, and undulations, offer retention of high loading and diffusion of Gu-, Ad-, and Th- nucleobases with multiple sensing durability. The signaling amplification and transduction of NMS for determination of trace levels of Gu-,

Ad-, and Th- nucleobases are evident. Our sensing design enables a low detection limit of 3.0 3, 0.36, and 0.34 nM for Gu, Ad, and Th, respectively, and a wide linear range of up to 1 µM. By controlling sensing condition assays, the NMS can sensibly and selectively monitor Gu-, Ad-, and Th- nucleobases in living cells exposed to oxidative stresses.

Scheme 1

2 Experimental Section

2.1 Non-metal sensory electrode design with B-doped carbon spherules

2.1.1 Synthesize of NMS of B-doped carbon spherules

An actively non-metal sensory electrode with B-doped carbon spherules surface was fabricated through a simple strategy. In general, NMS materials were formed after heat treatment at a high temperature by using α, D-glucose and different concentrations of boric acid. The glucose acts as carbon source, and boric acid acts as B atom source and directing agent. Boric acid plays a key role in the controlled formation of spherule construct with fused spheres, ridge end, and rugged surface. The following steps were followed for complete and facile formation of NMS. The solutions of 0.1 and 0.2 M boric acid are prepared by dissolving 0.5 (A) and 1 g (B) in 70 mL of deionized water (DI). The boric acid solutions were mixed with 0.2 M α, D-glucose solution. The two solutions with different concentrations of boric acid (A&B): α, D-glucose (1:2) and (1:1) were transferred into 100 mL Teflon-lined steel autoclave for HT (180 ºC for 24 h). After cooling, a brown precipitate was formed and washed by the solution of water/ethanol. The collected precipitates of various ratios were named as NMS-1, and NMS-2 and dried at 60 ºC for 24 h. For complete carbonization, NMS-1 and NMS-2 were annealed at 800 ºC under N_2 flow and step raise in temperature of 4 °C/min.

2.1.2 The fabrication of NMS electrode

The electrode modification to design NMS was assembled by following these steps: a) ink formation of NMS materials. The slurries of NMSs were prepared as follows. In brief, 5 mg

of NMS-1 and NMS-2 were dispersed in 1 mL of DI-water with 10% binder of poly(tetrafluoroethylene). b) The glassy carbon electrode (GCE, diameter 3.0 mm) was cleaned by polishing the electrode surface to be mirror like by using 0.05 μM alumina slurry followed by polishing in the diamond slurry. At every step, the electrodes were washed by DI-water every sweep. The electrode was sonicated in a solution of acetone and DI water for 30 min. c) Electrodes were formed with heterogeneous and spherule-rich interstitial core electrode surfaces. The designed electrodes of NMSs were set by the formation of a thin layer on the GCE surface by drop-casting 20 μL of NMS-1 and NMS-2, and then drying at room temperature. d) The designed electrodes were activated using continuous cyclic voltammetry sweeps for 10 cycles within the potential window of 0.0 – 1.8 V in 0.1 M NaOH at a scan rate of 0.1 Vs^{-1}.

2.2 Biological studies of the NMS in living cell interaction.

2.2.1 Cell culture of Hela and A549 cells.

Cell culture growth and passaging of HeLa and A549 cells were conducted. HeLa and A549 cells were passaged every 6-days and kept in an incubator under 5% CO_2 at 37 °C. The medium was changed two times a week throughout the lifetime of all cultures. The medium was prepared as follows: 50 mL of fetal bovine serum and 5 mL of antibiotic (penicillin/streptomycin) were added to 500 mL of Dulbecco's Modified Eagle's Medium.

2.2.2 Cytotoxicity, and cell imaging of Hela and A549 cells on NMS-2

The cytotoxicity of NMS-2 on HeLa cells was investigated using Cell Counting Kit-8 (CCK-8) assay. The cells (5×10^4 cells mL^{-1}) were moved onto 96-well microplates and kept in the incubator at 37 °C under 5% CO_2/95% air for 24 h. Various concentrations of NMS-2 were added (10 mL of 10, 20, 50, 100, and 200 μg mL^{-1}) to the cells medium, and incubated for 48 h. The CCK-8 solution (10 μL, 5 mg mL^{-1}) was added to each well and then incubated for 2 – 4 h. The incubated cells were measured using a microplate reader at an absorbance of 450 nm.

For visualization experiments using NMS-2, 5×10^4 cells mL^{-1} HeLa cells were seeded in glass bottom plate for 24 h and kept in the incubator. The cells were stained by phalloidin

488(1/500 mL) in PBS for F-actin staining and were stained by 4', 6-diamidino-2-phenylindole (DAPI) (1/1000 mL) in PBS for nuclear counter-staining for 5 min. The images of HeLa cells were captured at ambient temperature by confocal laser scanning microscopy (Leica TCS SPE5 X).

2.3 Real monitoring assay using NMS-2 to study the effect of oxidative stresses on living cells by sensing of Gu-, Ad-, and Th-DNA nucleobases

The effects of oxidative stresses on the cells was evaluated by the release of Gu-, Ad-, and Th- DNA nucleobases. In brief, 5×10^4 cell mL^{-1} HeLa and A549 cells were maintained in six-well plates and incubated for 3 days. After 3 days, the cell medium was changed, and mixed with Fenton solution ($FeSO_4.7H_2O$ and H_2O_2) and ascorbic acid, and then left for 6 h. For each six-well plate, 600 µL of 0.01 M $FeSO_4.7H_2O$ and 600 µL of 0.1 M ascorbic acid were added to 2.5 mL of the cell's medium, followed by 600 µL of 0.3 M H_2O_2. The supernatant was separated using a centrifuge prior to electrochemical cell measurement. 2.5 mL of the cell's medium was mixed with 7.5 mL of PBS (pH = 7.4) to be measured by electrochemical potentiostate using NMS-2 -modified electrode. The Fenton reagent induces the production of $2OH^{\bullet}$ from the reaction of Fe^{2+}/H_2O_2. The presence of ascorbic acid provides $2OH^{\bullet}$, which acts as the pro-oxidant of the reduction of Fe^{3+} into Fe^{2+}[42, 43] .

3 Results and discussion

3.1 NMS-2 with abundant interstitial core surface design for selective sensing of Gu-, Ad-, and Th- DNA nucleobases

Scheme S1 shows the synthesis of NMS of rich interstitial core surfaces. The non-metal sensory electrode structure model offers modulation of highly active interfacial surfaces with multiple architectonic configurations and geometrics and a mixture of various heterogeneous constructions. For instance, NMS-materials can be fabricated with multi-conjugated spheres structure. In addition, NMS structure with spherule units are designed with various geometric configurations such as nanospheres conjugated with curvature surface, grooves, and ridge end. The diverse alignment scales of NMS assemblies are designed using the developed

geometrical sensor to generate a highly sensitive and selective nano-sensor for screening Gu-, Ad-, and Th- DNA nucleobases with powerful molecular diffusion throughout out-/in- then up-/down-ward entrances and multiple discharge rates. NMS is designed with heterogeneous construct, rugged surface, B atoms doped with carbon-based materials, and nano-construct spherule shape to build a selective sensor model for simultaneous sensing of Gu-, Ad-, and Th- DNA nucleobases. In addition, a sensory protocol is proposed based on the B-doped carbon electrochemical sensor for detection of DNA nucleobases in living cells.

3.2 Controlled structural formation of NMS

The morphology of carbon-based materials of NMS was formed by boric acid as heteroatom dopant (B-atoms) and directing agent structure and α, D-glucose as a carbon source through hydrothermal treatment (HT). α, D-glucose was subjected to HT at high temperature (180 ºC) to a form microspherical carbon material. The glucose molecules were polymerized and aromatized to form a carbon chain network [30, 31]. Thus, the spherule structure of NMS was formed with high yield and in nanoscale after mixing D-glucose solution (0.2 M) and boric acid solutions (0.1 and 0.2 M). Boric acid and α, D-glucose chemically react to form a boronate ester between boric acids and α, D-glucose, and this ester is analogous to a carboxylate ester [44, 45]. Boronate ester acts as the initial monomer for polymerization, aromatization, and formation of a B-doped spherule structure. Boric acid is a source of heteroatom (boron atom) as dopant into the graphitic carbon network formation and as directing agent for direct control formation of a nano-spherule carbon structure. The synthesized NMS-materials were annealed at 800 ºC under N_2 flow for further carbonization and applied as electrocatalyst for electro-oxidation of DNA nucleobases such as Gu, Ad, and Th.

The morphology of NMS-materials was investigated using field-emission scanning electron microscope (FE-SEM, Figures 1A and S2A). The low-magnification FE-SEM-image of NMS-1 presents the formation of diverse types of carbon spheres in a nanosized scale with interlinked or/merged spheres (Figure S1Aa). Boric acid acted as a directing agent for the formation of nanosized carbon spheres. Other conformations of nanosized B-doped carbon

spherules with a rugged surface, grooves, and vortices are shown in Figure S1(b&c). The NMS-1 heterogeneous structures of dispersed nanospheres and conjugated spheres were observed to have curvature end and nanobuds. Figure S1Ac confirms the nanosphere's formation of NMS-1 with an average size of around 70 nm. The active doping and distribution of B atoms in carbon nanospheres were determined by EDX-SEM (Figure S1B). The atomic distributions of C, O, and B were determined by mapping each element. The homogeneous distribution and atomic content were evaluated. The surface components are 64.2% C (b), 23.24% O (c), and 12.56% B (d). The NMS-2 shaped spherule-rich interstitial core surfaces with heterogeneous composition and conjugated sphere structure were observed by FE-SEM (Figure 1A). The NMS-2 of spherule structure was formed from conjugated spheres linked horizontally with nano-construct, grooves, ridge end, and rugged surface [Figure 1A(a-c)]. Figure 1Ac presents the formation of nano-spherules with dispersed and interlinked spheres, indicating the formation of heterogeneous morphology with voids, grooves, and curvature ridges.

The complete profiles of NMS constructions and components were obtained using various characterization techniques, such as XRD, Raman shift, and N_2 adsorption-desorption isotherm. Figure 1B shows the WA-XRD pattern of NMS-1 (blue line) and NMS-2 (wine line). The XRD pattern exhibits two broad peaks centered at $2\Theta = 27.61°$ and 41.96°, thereby confirming the formation of carbon construct. Analysis of graphitic NMS-1 and NMS-2 electrode sphere surfaces indicated the formation of B-heteroatom through sp^2-graphitic interaction [46 –48]. Further confirmation of B-atoms participation in the carbon chain and distorted graphitic sp^2 hybridization, the Raman shift illustrates these characteristics (Figure 1C). The Raman spectrum of NMS-1 (Figure 1C, blue line) shows two strong bands at around 1337 and 1585 cm^{-1}, while a broad band appears at around 2633 cm^{-1} for D, G, and G^- bands, respectively. A small shift was observed in D, G, and G bands, centered at 1385, 1595, and 2620 cm^{-1}, respectively, for NMS-2 (Figure 1C, wine line). The D band shows the presence of heteroatoms, such as B and O atoms, in the graphitic carbon of NMS-2, indicating the distortion of the sp^2 graphitic chain, the formation of plane edge defects, and the presence of sp^3 hybridization. The I_D/I_G ratios are 0.76 and 0.84 for NMS-1 and NMS-2, respectively.

These values of I_D/I_G confirm the sp^2-hybridization distortion degree [48 –50]. Surface properties such as surface area, pore size, and pore volume of NMS-1 and NMS-2 are illustrated using N_2 adsorption–desorption isotherm. Figure 1(D&E) shows the N_2 adsorption–desorption isotherms of NMS-1 and NMS-2. The N_2 adsorption–desorption isotherms indicate the formation of micro- and mesoporous materials [51, 52]. The insets of Figure 1 (D&E) present the BJH pore size distribution and confirm the formation of hierarchical carbon construct with the presence of micro–mesopores distributions. The textural parameters of NMS electrodes in terms of porosity, pore volume, and surface area may indicate the facile surface diffusion of Gu-, Ad-, and Th- DNA nucleobases.

Figure 1Fa shows the HR-TEM image of NMS-2, confirming the presence of nano-spherical construct with fused nanospheres structure. The nano-spherical growth structure was further confirmed through high-magnification HR-TEM. The results confirm the nanosize of the spherical growth with an average size of 20–70 nm (Figure 1Fb). Focusing on the top view of the sphere ends confirmed the successful formation of nanosized carbon materials with rough texture and curvature ridges (Figure 1Fc). Boric acid acted as the directing agent for the controlled formation of B-doped carbon-based materials with heterogeneous surface and composition. Furthermore, the surface texture is rough with ridge end and grooves in between. Thus, heteroatom-doped nanocarbon-based materials were successfully developed through a simple approach using boric acid as a directing agent and as a B-atom source. The surface atomic components and distribution of NMS-2 are illustrated by dark-field (DF) EDS-STEM (Figure 1G). The EDS-STEM mapping confirms the homogeneous distribution of C, O, and B, with contents of 67.5, 16.9, and 15.6 wt.%, respectively (Figure 1G[b-d]). These results confirm the formation of B-doped nanocarbon based-materials with a homogeneous distribution of C, O, and B on the surface.

Figure 1

3.3 Electrochemical sensing protocol of Gu-, Ad-, and Th-DNA nucleobase

The electrochemical behavior of GCE, NMS-1, and NMS-2 was demonstrated using CV measurements in 1 mM $[Fe(CN)_6]^{3-/4-}$ (0.1 M KCl) in the potential range of 0.0–0.8 V within the scan rate of 0.1 Vs^{-1} [16, 18, 32]. The CV scans of $[Fe\ (CN)_6]^{3-/4-}$ on GCE (black line), NMS-1 (blue line), and NMS-2 (wine line) are presented in Figure 2A. The electron transfer velocity and effective electrode surface area of NMS proves the designed sensory protocol activity. The redox peaks difference (ΔE = the difference between the potential position of oxidation and reduction peak), and the current redox peak intensities reflect the charge transfer velocity and the effective electrode surface area. As shown in Figure 2A (wine line), the NMS-2 possesses the largest effective electrode surface area. The anodic current values of NMS-2, GCE, and NMS-1 are 36.35, 15.45, and 18.03 µA, respectively. Therefore, NMS-2 exhibits a large catalytic active surface area. In addition, the ΔE values of NMS-2, GCE, and NMS-1 are 125, 280, and 135 mV, respectively. NMS-2 exhibits the best electrochemical activity over the other electrodes tested. The induced electrochemical activity of NMS-2 may be related to the spherule-rich interstitial core surfaces, the heterogeneous surface of dispersed nanospheres, and the interconnected/fused nanospheres with high yield, rugged surface, grooves, ridge formation, and active doping of carbon chain by B atoms. Moreover, the presence of B atoms increases the number of vacant sites and edge defects in the carbon chain, enhances the electrochemical activity, and creates numerous active sites in the fabricated electrodes. The active doping of carbon materials by boron atoms decreases the level of Fermi energy and enhances the conductivity [53 –55].

Moreover, the effective surface area of the electrodes was calculated by applying Randles-Sevick formula as following [56]:

$$Ip(A) = 2.69\times10^5\ n^{3/2}\ A_0 D_0^{1/2} C_0 \nu^{1/2}$$

The Ip is the anodic peak current (A), n is number of the electron transfer, D is the diffusion coefficient ($cm^2\ s^{-1}$), C_o is the concentration of $[K_3Fe(CN)_6]$ (mol cm^{-3}), ν is the scan rate (V s^{-1}), and A is the electrode surface area (cm^2) . For 1.0 mM $[K_3Fe\ (CN)_6]$ in the 0.1 M KCl electrolyte: n = 1, D= 7.6×10^{-6} $cm^2\ s^{-1}$ [57]. Based on these data, the surface areas of the

electrodes are 0.066, 0.76, and 1.54 cm^2 for GCE, NMS-1, and NMS-2, respectively. Therefore, the effective doping of B-atoms enhances the electrocatalytic activity of the carbon-based materials of NMS-2 and induces the formation of highly active sensors with a large electrode surface area.

The electrochemical activities of GCE, NMS-1, and NMS-2 were further confirmed by impedance spectroscopy (EIS). EIS-analysis was conducted in 1 mM $K_3[Fe(CN)_6]$ solution to determine charge transfer velocity and electrode resistance. Figure 2B shows the Nyquist plot for GCE (black line), NMS-1 (blue line), and NMS-2 (wine line). The semicircle at high frequency represents electron transfer resistance (Res), and the line at low frequency represents electron diffusion of the designed electrode surface. As shown in Figure 2B, NMS-2 has the smallest semicircle and provides the lowest electron transfer resistance on its surface [18, 19, 30]. Furthermore, the electron diffusion on the surface of NMS-2 is the highest compared with the other electrodes [15–17, 20]. Therefore, NMS-2 exhibits a low charge resistance and a fast electron diffusion pathway. Thus, the active doping of the sp^2 carbon chain by B-atoms, the spherule-rich interstitial surface formation, micro–mesoporous network, and multi-diffusive centers lead to the formation of a high charge transport surface and facilitate electron diffusion on the designed sensor surface.

3.4 Signaling transduction of Gu-, Ad-, and Th-DNA nucleobases

Active interfacial surface based on NMS was designed for signaling Gu-, Ad-, and Th-DNA nucleobases. The electrocatalytic activity of Gu-, Ad-, and Th-DNA nucleobases on GCE, NMS-1, and NMS-2 was evaluated using CV in 0.1 M PBS (pH = 7.4) at a scan rate of 0.1 Vs^{-1}. Figure 2C shows the CV measurements of 20 µM Gu on GCE (black line), NMS-1 (blue line), and NMS-2 (wine line). A strong oxidation peak appears at an applied potential of 0.81 V on NMS-2 (wine line); meanwhile, abroad peak at high applied potential is found on GCE (black line), and a less strong peak appears on NMS-1 (blue line). The catalytic oxidation of 10 µM Ad and 10 µM Th on NMS-2 was evaluated. Strong oxidation peaks at applied potentials of 1.15 and 1.3 V are observed for Ad and Th, respectively. A low noticeable peaks are found on GCE, and less strong peaks are obtained on the NMS-1 (Figure

2[D&E]). Thus, NMS-2 could be a highly sensitive electrode for electro-oxidation of Gu-, Ad-, and Th-DNA nucleobases. The active signaling and selective monitoring of Gu-, Ad-, and Th-DNA nucleobases were studied using CV measurements at a scan rate of 0.1 Vs^{-1} in 0.1 M PBS (pH = 7.4) containing 10 µM Gu, 20 µM Ad, and 10 µM Th (Figure 2F). Three well-defined peaks are observed at applied potentials of 0.81, 1.15, and 1.3 V on NMS-1 (blue line) and NMS-2 (wine line), while low noticeable peaks appear for GCE (black line). A strong signal with high current values for electro-oxidation of Gu-, Ad-, and Th-DNA nucleobases on NMS-2 indicates the high sensitivity and selectivity of the designed sensor. The active doping of the carbon chain by B atoms leads to a surface construct with spherule structure with grooves, rugged surface, and ridge end. Hence, NMS-2 could be a supreme sensor for simultaneous detection of Gu-, Ad-, and Th-DNA nucleobases.

Figure 2

The pH of the supporting electrolyte plays a key role in sensitive and selective signaling of Gu, Ad, and Th-DNA nucleobases and in the overall electro-oxidation process. The pH-dependent signaling of 10 µM Gu and 10 µM Ad in 0.1 PBS within the pH range of 6–9 was studied using CV at the scan rate of 0.1 Vs^{-1} on NMS-2. As shown in Figure 3(A&C), the anodic signal strength and applied potential of Gu and Ad changes as pH varies from 6 to 9. In addition, the anodic applied potential shifts negatively, confirming the participation of protons in the overall electro-oxidation process. A linear relationship was observed from the plotting of pH versus applied potential (V) with the regression equations of E (mV) = 1.37 – 0.066 pH and E (mV) = 1.55 – 0.050 pH for Gu and Ad, respectively (Figure 3[B&D]). The slopes of these linear equations are near the theoretical Nernst value (59 mV). Therefore, the overall process is conducted with proton number equal to the electron number, and the overall electro-oxidation process follows $4e^-/4H^+$. The effect of pH on the anodic signal and applied potential position for Th (50 µM) was obtained within varying pH of 6 to 7.4 (Figure 3E). The anodic applied potential shifts negatively with varying pH. Based on the plot of pH versus E(V), a linear relationship is obtained with regression equation of pH = 1.73 – 0.056E (mV) (Figure 3F). The slope value supports the overall electro-oxidation process to follow

the mechanism $2e^-/2H^+$ [1, 58,59]. The anodic signal strength of Gu, Ad, and Th changes with varying pH (Figure 3[A, C, and D]). The optimum pH is 7.4 (near the physiological pH) [15, 18].

The electro-oxidation kinetic process of Gu-, Ad-, and Th-DNA nucleobases on the surface of NMS-2 was investigated using CVs in 0.1 M PBS (pH =7.4) at scan rates of 50 – 250 Vs^{-1}. Figure 3G shows the CVs of 40 µM Gu at various scan rates. The anodic peak current increases as the scan rate increases from 50 Vs^{-1} to 250 Vs^{-1}. The kinetic interaction of Gu on the electrode surface of NMS-2 is obtained from the linear equation of scan rate (mVs^{-1}) versus current (µA) with regression equation of I (µA) = 97.03 + 0.002 ν (mVs^{-1}), R^2 = 0.997 (Figure 3J). The scan rate effect of 100 µM Th was determined in 0.1 PBS (pH = 7.4) (Figure 3I). With increasing the scan rate, the anodic peak current increases. The relationship between scan rate (mVs^{-1}) and anodic current (µA) for Th molecules follows the linear regression equation of I (µA) = 57.72 + 0.006 ν (mVs^{-1}), R^2 = 0.96 (Figure 3L). Thus, the kinetic mechanism on the surface of NMS-2 for electro-oxidation of Gu and Th is a controlled adsorption process [18,19]. The kinetic mechanism for electro-oxidation of Ad on the NMS-2 surface is a diffusion-controlled process. This result was confirmed by studying the scan rate effect on the anodic signaling of 20 µM Ad. By plotting the square root of scan rate versus the anodic peak current, a linear relationship is obtained with a regression equation of I (µA) = -63.7 + 0.046 ν (mVs^{-1}), R^2 = 0.995 (Figure 3[H&K]) [15, 60, 61].

Figure 3

3.6 Simultaneous and selective signaling of Gu-, Ad-, and Th-DNA nucleobases using NMS protocol

Simultaneous and selective detection of Gu, Ad, and Th was conducted using the designed NMS sensor. The sensitivity and selectivity of NMS-2 for detection of DNA nucleobases were measured using SWV measurements in 0.1 M PBS (pH = 7.4). Individual monitoring of one target in the presence of the other targets was performed in a ternary mixture of Gu, Ad, and Th. The concentration of one target is increased while keeping the concentration of the other targets' constant (Figure 4). Figure 4Aa shows the results of SWV measurements

of various concentrations of Gu ranging from 0.1 μM to 1 μM in the presence of Ad (0.04 μM) and Th (40 μM). The anodic current of Gu increases with increasing concentration of DNA-nucleobases. Based on the plot of [Gu](μM) and current (μA), a linear relationship is obtained at low concentrations with the regression equation of I(μA) = 1.48 + 0.019 $\times 10^{-3}$ [Gu] (μM), R^2 = 0.999 (S/N = 3). Meanwhile, the linearity is distorted at high concentrations, which may be related to the saturation of the electrode surface due to the controlled adsorption mechanism (Figure 4Ba). The limit of detection is 3.0 nM (based on the 3α/s) (where α is intercept standard error, and s is the slope value). NMS-2 could be a highly sensitive sensor for selective signaling of Gu in the presence of Ad and Th. The sensitivity and selectivity of the sensor for detection of Ad and Th were illustrated using SWV measurements. With increasing Ad concentrations, the anodic current increases within 0.04–0.8 μM in the presence of 0.1 μM Gu and 40 μM Th (Figure 4Ab). Moreover, the same result is obtained for Th-molecules. The current response increases with increasing Th-concentrations within the range of 0.05–0.5 μM in the presence of 0.1 μM Gu and 0.1 μM Ad (Figure 4Ac). Linear relationships are observed from plotting Ad- and Th-concentrations (M) against the response current (μA) with regression equations of I(μA) = 2.8 + 0.025 $\times 10^{-3}$ [Ad] (μM), R^2 = 0.969 (S/N = 3) and I(μA) = 5.43 + 0.043 $\times 10^{-3}$ [Th] (μM), R^2 = 0.96 (S/N = 3). The limits of detection are 0.36 and 0.34 nM for Ad and Th based on 3α/s relationship, respectively (Figure 4B [b&c]). This finding indicates the potential of the electrochemical sensor developed based on NMS for highly sensitive detection of Gu-, Ad-, and Th-DNA nucleobases with facile stability, and low detection limit.

The simultaneous highly sensitive and selective detection of Gu-, Ad-, and Th-DNA nucleobases was conducted to establish a sensing protocol. Figure 4C shows well-defined three peaks at applied potentials of 0.8, 1.1, and 1.27 V for the electro-oxidation of Gu-, Ad-, and Th-DNA nucleobases on the NMS-2, respectively. The ability of the designed electrode for detection of all targets in one step and high selectivity is confirmed based on ΔE values between all targets. Sensitivity was evaluated by adding Gu-, Ad-, and Th-DNA nucleobases and measuring the anodic current peak. As shown in Figure 4C, the anodic current peak increases linearly with increasing concentrations of Gu (0.25–3 μM), Ad (0.25–3 μM), and

Th (0.5–10 μM). The regression equations of the three DNA nucleobases are I(μA) = 1.38 + 1.1 [Gu] (μM), R^2 = 0.948 (S/N = 3); I(μA) = 2.79 + 1.74 [Ad] (μM), R^2 = 0.967 (S/N = 3); and I(μA) = 5.05 + 0.897 [Th] (μM), R^2 = 0.994 (S/N = 3) for Gu, Ad, and Th, respectively. Based on the calibration curves presented in the inset of Figure C, the limit of detection values are as low as 56, 46, and 145 nM for Gu, Ad, and Th based on 3σ/s, respectively. The amperometry responses of various concentrations of Gu, Ad, and Th at fixed applied potential are presented in Figure 4D to confirm the sensitivity and selectivity of the designed sensor. The time–current response was evaluated using Gu (20 nM) at a fixed applied potential of 0.8 V, Ad (50 nM) at a fixed applied potential of 1.1 V, and Th (100 nM) at a fixed applied potential of 1.3 V.

The selectivity of the NMS sensor towards Gu-, Ad-, and Th- DNA nucleobases was investigated using SWV-, and CA-techniques (Figure S2). According to SWV sensing protocol based on tertiary mixture components (i.e., Gu, Ad and Th DNA-nucleobases in one single screen), well resolved three peaks are obtained with (i) high peak-to-peak separation and (ii) sensitive responses (Figure 4C). The ΔE values of 300, 200, and 500 mV for Gu-Ad, Ad-Th, and Gu-Th, respectively, confirm the highly selective detection of Gu-, Ad-, and Th-DNA nucleobases using NMS-2 sensor. The selectivity assay of Gu, Ad, and Th was performed using CA-response in the presence of various interfering molecules of K^+ (0.1 mM), Na^+ (0.5 mM), 0.5 mM ascorbic acid (AA), 0.5 mM Glucose (Gl), 0.5 mM tryptophan (Tr), 0.5 mM H_2O_2, and 0.5 mM glutamine (Glu). Figure S2 shows that the sensitive and selective responses of Gu-, Ad-, and Th-DNA nucleobases can be achieved at specifically applied potential of 0.8. 1.1, and 1.3 V, respectively. The CA assay gives evidence that the NMS-2 shows high selectivity of Gu-, Ad-, and Th- DNA nucleobases in the presence of very competitive substances and species. Table S1 represents the sensing parameters of the various electrodes compared with our NMS-2-modified electrode during the detection of Gu-, Ad-, and Th- DNA nucleobases. The NMS-2 is highly sensitive electrode design with wide linear range among all reported electrodes. The finding indicates that the designed NMS-2 sensor has high stability, and excellent sensitivity and selectivity during the monitoring assay of Gu-, Ad-, and Th- DNA nucleobases.

Figure 4

3.7 Viability and biocompatibility to living cells

In vitro and in vivo assays for detection of DNA nucleobases in human fluids and liberated cells exposed to oxidative stresses are highly required for clinical investigations and maintaining quality human health. The material–cell interaction indicates the viability and biocompatibility of the materials. HeLa and A549 cell lines represent the models for cervical and lung cancer diagnosis and for living cells [62]. The biocompatibility of NMS-2 in HeLa cells line was evaluated using confocal microscope (Leica Microsystems LAS AF-TCS MP5). The results show the cell images of HeLa cells incubated with 40 µg/mL NMS-2 for 2 h and stained by DAPI and phalloidin for nucleus and F-actin counterstaining, respectively (Figure 5). Figure 5A shows the bright-field image of HeLa cells with NMS-2. NMS-2 exists around the cells. Figure 5(B &C) illustrates the F-actin and nucleus of HeLa cells, indicating the cytoskeleton and nucleus without damage or shrinkage of the cell's morphology. The merged cell image (Figure 5D) confirms the cell morphology and biocompatibility of NMS-2. These results provide a basis for the in vivo studies of the designed materials. Cell viability and biocompatibility were determined using cell sorter analysis. Figure 5(E&F) shows the dot plots of FACS for control and cells incubated with 40 µg/mL NMS-2 for 2 h, with cell's percentages of 99.87% and 79.77%, respectively. The percentage of leukocytes/monocytes is 79.77% from the dot plot, confirming the high cell diffusion in the presence of NMS-2 [63, 64]. Thus, NMS-2 shows low cytotoxicity and high cell viability and biocompatibility. The cell viability and cytotoxicity of HeLa cells in the presence of NMS-2 were confirmed by the FITC plot and the cell counting kit-8 (CCK-8) assay [65, 66]. Figure S3(A&B) shows the FITC plot for control and incubated cells with NMS-2. The high cell viability confirms the low cytotoxicity of NMS-2. The CCK-8 cell viability assay was performed after incubation of HeLa cells with various concentrations of NMS-2 (20-200 µg/mL) for 24 h at 37 °C. Figure S3C shows the column plot of NMS-2 concentration versus cell viability. NMS-2 achieves high cell viability, losing only 0.7% cells at 20 µg/mL and only 5% at 200 µg/mL.

These results confirm the high biocompatibility and low cytotoxicity of NMS-2 on living cells and can be used for in vivo and in vitro studies.

Figure 5

3.8 Controlled monitoring of Gu-, Ad-, and Th- DNA nucleobases from oxidative DNA in living cells

Oxidative stresses in living cells cause damages to DNA, leading to cell mutation and aging [6]. The oxidative stresses generate free radicals (i.e., formulation of OH• radicals), which causes DNA oxidation and damage. Therefore, DNA nucleobases, namely, Gu, Ad, Th, and cytosine and their oxidized forms are liberated [39]. NMS-2 can sensitively and selectively screen ultra-low concentrations of Gu, Ad, and Th in one step. To determine the effect of oxidative stress on living cells, we used two types of cells (HeLa and A549 cells). The cells were passaged and incubated in a humidified chamber of 5% CO_2 at 37 °C. HeLa and A549 cells (5×10^4 cells mL^{-1}) were kept in six-well plates, incubated for 72 h, and added with 600 µL of Fenton reagent + 600 µL of AA. The cells were left for 4 h before the electrochemical detection test. The supernatant was tested for detection of DNA nucleobases and their oxidized forms liberated from damaged DNA in living cells. Figure 5 (G&H) shows the SWV measurements of the supernatant of cells treated with Fenton reagent and untreated cells (control cells). Figure 5G shows the SWV measurement of the supernatant of HeLa cells after exposure to oxidative stresses, such as OH-radical. Three well-defined peaks are seen at 0.73, 1.04, and 1.12 V for Gu, Ad, and Th, respectively. The three peaks of DNA nucleobases appear at 0.73, 1.04, and 1.12 V after scanning the supernatant of A549 cells exposed to the oxidative stress of OH-radical (Figure 5H). Both types of cells exposed to the Fenton reagent liberate DNA nucleobases, providing evidence of the effect of oxidative damage on DNA in living cells. NMS-2 can sensitively and selectively detect Gu, Ad, and Th liberated from living cells after exposure to oxidative stresses, such as ROS, without any effect of interference and in high stability. Thus, NMS-2 can be used to evaluate DNA damage in living cells and could be used for healthcare quality profile.

3.9 Reproducibility of NMS sensors

Highly stable and efficient reproducible electrodes are a crucial factor that determines the validity of the electrode and its economical use. The stability and reusability of NMS-2 were tested using SWV. The reusability of NMS-2 was confirmed after plotting the current response as a function of five samples at fixed concentrations of 0.05 µM Gu, 0.05 µM Ad, and 10 µM Th. All measurements were repeated after washing NMS-2 with distilled H_2O for three times under the optimal sensing conditions (Fig. 6[A, B, and C]). Thus, NMS-2 provides high sensing response efficiency (i.e., 99%), despite five reuses/cycles with RSD values of 1.6 %, 3.2 %, and 3.2 % for Gu, Ad, and Th respectively. Current response was examined for a multiple of five electrodes from NMS-2 at a concentration of 0.1 µM Gu, 0.1 Ad, and 40 µM. The RSDs of the five SWV measurement assays for Gu, Ad, and Th are within 1.3%–2.18%, as evidenced by the plot of the electrode number versus the response current [Figure 6(D, E, and F)]. In addition, the NMS-2 stability for measuring of [Gu] (0.5 µM), [Ad] (0.5 µM), and [Th] (0.5 µM) was studied after storage the electrode for 12 days, and the measurement was performed using SWV every 3 days. Form Figure 6 (G-I), the NMS-2 show highly stable electrode after several measurements for a prolonged time with losing of 4.6 %, 4.4 %, and 3.7 % from their initial values of Gu, Ad, and Th response (after 12 days), respectively. Therefore, the designed electrode based on NMS-2 could be used as a highly stable and reproducible sensor for sensitive and selective signaling of Gu, Ad, and Th. Thus, the facile diffusion of Gu, Ad, and Th and the heterogeneous surface construction with a rugged surface, grooves, ridge end, and spherule shape with abundant core interstitial surface, and active doping by B atoms lead to the formation of a highly stable and reproducible electrode with facile sensitivity and selectivity

Figure 6

Conclusion

This work presents the controlled fabrication of electrochemical sensors based on NMS for selective monitoring of Gu, Ad, and Th in living cells. NMS surfaces are formed with spherule construct of heterogeneous composition and abundant interstitial core surface. The NMS surface is fabricated from conjugated and interconnected nano-spheres with rugged surface texture and an average width size of 70 nm. The robustness, and inner pore cavities, of spherule structures and grooves create an ideal sensor with high durability and multi-diffusive rate kinetics. The design of an electrochemical sensor based on B-doped carbon materials creates a highly active electrode surface with abundant central active sites, curvature surface topography, and anisotropic spherule geometry. The electrode has low surface resistance and high electron diffusion and could be used for sensing of Gu, Ad, and Th in living cells. NMS shows active signaling transduction for sensing Gu, Ad, and Th individually and simultaneously. The designed nano-sensor of NMS provides an ultrasensitive sensor for signaling trace concentrations of DNA nucleobases with low detection limits of 3.0, 0.36, and 0.34 nM for Gu, Ad, and Th, respectively, and a wide linear range of up to 1 μM. The designed sensor based on NMS is used to establish a highly efficient sensor for evaluating abnormal human metabolism as a function of DNA damage. NMS provides highly stable constructed materials with nano-construction, low cytotoxicity, high biocompatibility, and facile viability. NMS successfully detects Gu, Ad, and Th from damaged DNA in living cells. NMS could be a sensitive sensor for evaluating DNA damage with high sensitivity and selectivity, reasonable stability, and efficient reproducibility with RSD up to 3.2 %. NMS can be used for DNA damage evaluation in living cells and for some related diseases, such as cancer.

ACKNOWLEDGMENTS

This work was supported by the Japan Society for the Promotion of Science (JSPS), grant No. P19067.

References

1. M. Arvand, M.S. Ardaki, Poly-l-cysteine/electrospun copper oxide nanofibers-zinc oxide nanoparticles nanocomposite as sensing element of an electrochemical sensor for simultaneous determination of adenine and guanine in biological samples and evaluation of damage to dsDNA and DNA purine bases by UV radiation, Anal. Chim. Acta, 986 (2017) 25-41. https://doi.org/10.1016/j.aca.2017.07.057

2. K.L. Ng, S.M. Khor, Graphite-Based Nanocomposite Electrochemical Sensor for Multiplex Detection of Adenine, Guanine, Thymine, and Cytosine: A Biomedical Prospect for Studying DNA Damage, Anal. Chem. 89 (2017) 10004-10012 (2017). https://doi.org/10.1021/acs.analchem.7b02432

3. M.L. Ribeiro, D.G. Priolli, D.D. Miranda, D.P. Arçari, J. Pedrazzoli Jr, C.A. Martinez, Analysis of oxidative DNA damage in patients with colorectal cancer, Clin. colorectal cancer, 7 (2008) 267-272. https://doi.org/10.3816/CCC.2008.n.034

4. M. S. Lowenthal, E. Quittman, K. W. Phinney, Absolute Quantification of RNA or DNA Using Acid Hydrolysis and Mass Spectrometry, Anal. Chem. 91, 22 (2019) 14569–14576. https://doi.org/10.1021/acs.analchem.9b03625

5. A. Bonanni, M. Pumera, Graphene platform for hairpin-DNA-based impedimetric genosensing, ACS Nano, 5 (2011)2356-2361 (2011). https://doi.org/10.1021/nn200091p

6. S.A. El-Safty, M.A. Shenashen, Advanced nanoscale build-up sensors for daily life monitoring of diabetics, Adv. Mater. Interfaces, 7(15) (2020) 2000153. https://doi.org/10.1002/admi.202000153

7. S.A. El-Safty, M.A. Shenashen, Nanoscale dynamic chemical, biological sensor material designs for control monitoring and early detection of advanced diseases, Mater. Today Bio, 5 (2020) 100044. https://doi.org/10.1016/j.mtbio.2020.100044

8. K.-J. Huang, H.-L. Shuai, Y.-X. Chen, Layered molybdenum selenide stacking flower-like nanostructure coupled with guanine-rich DNA sequence for ultrasensitive ochratoxin A

aptasensor application, Sens. Actuators B, 225 (2016) 391-397. https://doi.org/10.1016/j.snb.2015.11.070

9. A. Erdem, M. Muti, P. Papakonstantinou, E. Canavar, H. Karadeniz, G. Congur, S. Sharma, Graphene oxide integrated sensor for electrochemical monitoring of mitomycin C–DNA interaction, Analyst, 137 (2012) 2129-2135. https://doi.org/10.1039/C2AN16011K

10. F. Yang, J. Guan, S.P. Li, Fast simultaneous determination of 14 nucleosides and nucleobases in cultured Cordyceps using ultra-performance liquid chromatography, Talanta, 73 (2007) 269-273. https://doi.org/10.1016/j.talanta.2007.03.034

11. D.P. Glavin, H.J. Cleaves, A. Buch, M. Schubert, A. Aubreyb, J.L. Bada, P.R. Mahaffy, Sublimation extraction coupled with gas chromatography-mass spectrometry: a new technique for future in situ analyses of purines and pyrimidines on Mars, Planet Space Sci. 54 (2006) 1584-1591. https://doi.org/10.1016/j.pss.2005.12.023

12. S. Pang, Y. Zhang, C. Wu, S. Feng, Fluorescent carbon dots sensor for highly sensitive detection of guanine, Sens. Actuators B, 222 (2016) 857-863. https://doi.org/10.1016/j.snb.2015.09.037

13. A.M. de Carvalho, A.A.F. Carioca, R.M. Fisberg, L. Qi, D.M. Marchioni, Joint association of fruit, vegetable, and heterocyclic amine intake with DNA damage levels in a general population, Nutrition, 32 (2016) 260-264. https://doi.org/10.1016/j.nut.2015.08.018

14. F.-Q. Yang, L. Ge, J.W.H.Yong, S.N. Tan, S.-P Li, Determination of nucleosides and nucleobases in different species of Cordyceps by capillary electrophoresis–mass spectrometry, J. Pharm. Biomed. Anal. 50 (2009) 307-314. https://doi.org/10.1016/j.jpba.2009.04.027

15. N. Akhtar, M.Y. Emran, M.A. Shenashen, H. Khalifa, T. Osaka, A. Faheem, T. Homma, H. Kawarada, S. A. El-Safty, Fabrication of photo-electrochemical biosensors for ultrasensitive screening of mono-bioactive molecules: the effect of geometrical structures

and crystal surfaces, J. Mater. Chem. B, 5 (2017) 7985-7996. https://doi.org/10.1039/C7TB01803G

16. M.Y. Emran, H. Khalifa, H. Gomaa, M. A. Shenashen, N. Akhtar, M. Mekawy, A. Faheem, S. A. El-Safty, Hierarchical CN doped NiO with dual-head echinop flowers for ultrasensitive monitoring of epinephrine in human blood serum, Microchim. Acta,184 (2017) 4553-4562. https://doi.org/10.1007/s00604-017-2498-3

17. M.Y. Emran, M. Mekawy, N. Akhtar, M. A. Shenashen, I. M. El-Sewify, A. Faheem, S. A. El-Safty, Broccoli-shaped biosensor hierarchy for electrochemical screening of noradrenaline in living cells, Biosens. Bioelectron. 100 (2018) 122-131. https://doi.org/10.1016/j.bios.2017.08.050

18. M.Y. Emran, M.A. Shenashen, A.A. Abdelwahab, M. Abdelmottaleb, M. Khairy, S. A. El-Safty, Nanohexagonal Fe2O3 Electrode for One-Step Selective Monitoring of Dopamine and Uric Acid in Biological Samples, Electrocatalysis, 9(4), (2018) 514-525 (2018). https://doi.org/10.1007/s12678-018-0468-0

19. M.Y. Emran, M.A. Shenashen, A.A. Abdelwahab, H. Khalifa, M. Mekawy, N. Akhtar, M. Abdelmottaleb, S. A. El-Safty, Design of hierarchical electrocatalytic mediator for one step, selective screening of biomolecules in biological fluid samples, J. Appl. Electrochem. 48(5) (2018) 529-542. https://doi.org/10.1007/s10800-018-1175-5

20. M.Y. Emran, M.A.Shenashen, M. Mekawy, A. M. Azzam, N. Akhtar, H. Gomaa, M. M. Selim, A. Faheem, S. A. El-Safty, Ultrasensitive in-vitro monitoring of monoamine neurotransmitters from dopaminergic cells, Sens. Actuators B, 259 (2018)114-124. https://doi.org/10.1016/j.snb.2017.11.156

21. T.S. Ortolani, T.S. Pereira, M.H. Assumpção, F.C. Vicentini, G.G. de Oliveira, B.C. Janegitz,. Electrochemical sensing of purines guanine and adenine using single-walled carbon nanohorns and nanocellulose, Electrochim. Acta, 298 (2019) 893-900. https://doi.org/10.1016/j.electacta.2018.12.114

22. B. Hu, J. Huang, L. Wang, One-Dimensional Nanowire Hybrids Constructed from Silver Nanowire and Carboxylic Multi-Walled Carbon Nanotubes for Electrochemical Simultaneous Determination of Guanine and Adenine, ChemistrySelect, 3 (2018) 8514-8521 (2018). https://doi.org/10.1002/slct.201801613

23. X. Tu, X. Luo, S. Luo, L. Yan, F. Zhang, Q. Xie, Novel carboxylation treatment and characterization of multiwalled carbon nanotubes for simultaneous sensitive determination of adenine and guanine in DNA, Microchim. Acta, 169 (2010) 33-40 (2010). DOI 10.1007/s00604-010-0307-3

24. H. Tian, L. Wang, Z. Sofer, M. Pumera, A. Bonanni, Doped graphene for DNA analysis: The electrochemical signal is strongly influenced by the kind of dopant and the nucleobase structure, Sci. Rep. 6 (2016) 33046. https://doi.org/10.1038/srep33046

25. S. Pruneanu, A.R. Biris, F. Pogacean, M. Coroş, G.K. Kannarpady, F. Watanabe, A.S. Biris, The study of adenine and guanine electrochemical oxidation using electrodes modified with graphene-platinum nanoparticles composites, Electrochim. Acta, 139 (2014) 386-393. https://doi.org/10.1016/j.electacta.2014.06.163

26. A.A. Ensafi, M.M. Abarghoui, B. Rezaei, A new electrochemical sensor based on porous silicon supported Pt–Pd nanoalloy for simultaneous determination of adenine and guanine, Sens. Actuators B, 204 (2014) 528-535. https://doi.org/10.1016/j.snb.2014.08.009

27. L. Zhang, J. Zhang, Multiporous molybdenum carbide nanosphere as a new charming electrode material for highly sensitive simultaneous detection of guanine and adenine, Biosens. Bioelectron. 110 (2018) 218-224. https://doi.org/10.1016/j.bios.2018.03.064

28. J. Huang, Y. Liu, T. You, Carbon nanofiber based electrochemical biosensors: A review, Anal. Meth. 2 (2010) 202-211. https://doi.org/10.1039/B9AY00312F

29. W. Yang, K.R. Ratinac, S.P. Ringer, P. Thordarson, J.J. Gooding, F. Braet, Carbon nanomaterials in biosensors: should you use nanotubes or graphene?, Ang. Chem. Int. Ed. 49 (2010) 2114-2138. https://doi.org/10.1002/anie.200903463

30. M.Y. Emran, M.A. Shenashen, A.A. Abdelwahab, M. Abdelmottaleb, S.A. El-Safty, Facile synthesis of microporous sulfur-doped carbon spheres as electrodes for ultrasensitive detection of ascorbic acid in food and pharmaceutical products. New J. Chem. 42 (2018) 5037-5044. https://doi.org/10.1039/C7NJ05047J

31. M.Y. Emran, M.A. Shenashen, H. Morita, S.A. El-Safty, One-step selective screening of bioactive molecules in living cells using sulfur-doped microporous carbon. Biosen. Bioelectron. 109 (2018) 237-245. https://doi.org/10.1016/j.bios.2018.03.026

32. M.Y. Emran, M.A. Shenashen, H. Morita, S.A. El-Safty, 3D-Ridge Stocked Layers of Nitrogen-Doped Mesoporous Carbon Nanosheets for Ultrasensitive Monitoring of Dopamine Released from PC12 Cells under K+ Stimulation, Adv. Healthcare Mater. 7 (16) (2018) 1701459. https://doi.org/10.1002/adhm.201701459

33. M.Y. Emran, S.A. El-Safty, M.A. Shenashen, T. Minowa, A well-thought-out sensory protocol for screening of oxygen reactive species released from cancer cells. Sens. Actuators B, 284 (2019) 456-467. https://doi.org/10.1016/j.snb.2018.12.142

34. T. Chen, L. Pan, T. Loh, D. Chua, Y. Yao, Q. Chen, D. Li, W. Qin, Z. Sun, Porous nitrogen-doped carbon microspheres as anode materials for lithium ion batteries, Dalton Trans. 43 (2014) 14931-14935. https://doi.org/10.1039/C4DT01223B

35. Q. Liu, H.Tian, Z. Dai, *H. Sun*, J. Liu, Z. Ao, S. Wang, C. Han, S. Liu, Nitrogen-doped Carbon Nanospheres-Modified Graphitic Carbon Nitride with Outstanding Photocatalytic Activity, Nano-Micro Lett. 12 (2020) 24. https://doi.org/10.1007/s40820-019-0358-x

36. K. Xiao, Y. Liu, P.a. Hu, G. Yu, Y. Sun, D. Zhu, n-Type field-effect transistors made of an individual nitrogen-doped multiwalled carbon nanotube, J. Am. Chem. Soc. 127 (2005) 8614-8617. https://doi.org/10.1021/ja042554y

37. L. K. Putri, B.-J. Ng, W.-J. Ong, H. W. Lee, W. S. Chang, S.-P. Chai, Engineering nanoscale p–n junction via the synergetic dual-doping of p-type boron-doped graphene

hybridized with n-type oxygen-doped carbon nitride for enhanced photocatalytic hydrogen evolution, J. Mater. Chem. A, 6 (2018) 3181-3194. https://doi.org/10.1039/C7TA09723A

38. Y. Lin, S. Wu, W. Shi, B. Zhang, J. Wang, Y.A. Kim, M. Endo, D.S. Su, Efficient and highly selective boron-doped carbon materials-catalyzed reduction of nitroarenes, Chemical Communications, 51 (2015) 13086-13089. https://doi.org/10.1039/C5CC01963J

39. Y. Fang, I. S. Merenkov, X. Li, J. Xu, S. Lin, M. L. Kosinova, X. Wang, Vertically aligned 2D carbon doped boron nitride nanofilms for photoelectrochemical water oxidation, J. Mater. Chem. A, 8 (2020)13059-13064. https://doi.org/10.1039/D0TA04593D

40. S. Shiraishi, M. Kibe, T. Yokoyama, H. Kurihara, N. Patel, A. Oya, Y. Kaburagi, Y. Hishiyama, Electric double layer capacitance of multi-walled carbon nanotubes and B-doping effect, Appl. Phys. A, 82 (2006) 585-591. https://doi.org/10.1007/s00339-005-3399-6

41. B. Wang, K.K. Ostrikov, T. van der Laan, R. Shao, L. Li, Structure and photoluminescence of boron-doped carbon nanoflakes grown by hot filament chemical vapour deposition, J. Mater. Chem. C, 3 (2015) 1106-1112. https://doi.org/10.1039/C4TC01974A

42. P. Wang, H. Wu, Z. Dai, X. Zou, Simultaneous detection of guanine, adenine, thymine and cytosine at choline monolayer supported multiwalled carbon nanotubes film. Biosens. Bioelectron. 86 (2011) 671-676. https://doi.org/10.1016/j.bios.2011.01.011

43. J. Cross, R. Currier, D. Torraco, L. Vanderberg, G. Wagner, P. Gladen, Killing of Bacillus spores by aqueous dissolved oxygen, ascorbic acid, and copper ions, Appl. Environ. Microbiol. 69 (2003) 2245-2252. DOI:10.1128/AEM.69.4.2245-2252.2003

44. S. Jin, Y. Cheng, S. Reid, M. Li, B. Wang, Carbohydrate recognition by boronolectins, small molecules, and lectins, Med. Res. Rev. 30 (2010) 171-257. https://doi.org/10.1002/med.20155

45. B. Pappin, M.J. Kiefel, T.A. Houston, Boron-carbohydrate interactions. Carbohydrates-Comprehensive Studies on Glycobiology and Glycotechnology: InTech 2012. http//dx.doi.org/10.5772/50630

46. D. Hassen, M. A. Shenashen, A. R. El-Safty, A. Elmarakbi, S.A. El-Safty, Anisotropic N-Graphene-diffused Co3O4 nanocrystals with dense upper-zone top-on-plane exposure facets as effective ORR electrocatalysts, Sci. Rep. 8 (2018) 3740. https://doi.org/10.1038/s41598-018-21878-w

47. D.M. Fernandes, M. Costa, C. Pereira, B. Bachiller-Baeza, I. Rodríguez-Ramos, A. Guerrero-Ruiz, C. Freire, Novel electrochemical sensor based on N-doped carbon nanotubes and Fe3O4 nanoparticles: Simultaneous voltammetric determination of ascorbic acid, dopamine and uric acid, J. Coll. interface Sci. 432 (2014) 207-213. https://doi.org/10.1016/j.jcis.2014.06.050

48. S. Ge, J. He, C. Ma, J. Liu, F. Xi, X. Dong, One-step synthesis of boron-doped graphene quantum dots for fluorescent sensors and biosensor. Talanta, 199 (2019) 581-589. https://doi.org/10.1016/j.talanta.2019.02.098

49. M.S. Selim, S.A. El-Safty, M.A. Shenashen, M.A. El-Sockary, O.M. Abo Elenien, A. M. EL-Saeed, Robust alkyd/exfoliated graphene oxide nanocomposite as a surface coating, Prog. in Org.Coatings,126 (2019) 106-118. https://doi.org/10.1016/j.porgcoat.2018.09.032

50. P. Niedziałkowski, Z. Cebula, N. Malinowska, W. Białobrzeska, M. Sobaszek, M. Ficek, R. Bogdanowicz, J.S. Anand, T. Ossowski, Comparison of the paracetamol electrochemical determination using boron-doped diamond electrode and boron-doped carbon nanowalls. Biosens. Bioelectron.126 (2019) 308-314. https://doi.org/10.1016/j.bios.2018.10.063

51. N. Akhtar, S.A. El-Safty, M.E. Abdelsalam, M.A. Shenashen, H. Kawarada, Radially oriented nanostrand electrodes to boost glucose sensing in mammalian blood, Biosens. Bioelectron. 77, (2016) 656-665. https://doi.org/10.1016/j.bios.2015.10.023

52. H. Khalifa, S.A. El-Safty, A.Reda, M. A. Shenashen, M. M. Selim, A. Elmarakbi, H. A. Metawa, Theoretical and Experimental Sets of Choice Anode/Cathode Architectonics for High-Performance Full-Scale LIB Built-up Models, Nano-Micro Lett. 11 (2019) 84. https://doi.org/10.1007/s40820-019-0315-8

53. J.S. Burgess, C.K. Acharya, J. Lizarazo, N. Yancey, B. Flowers, G. Kwon, T. Klein, M. Weaver, A.M. Lane, C.H. Turner, Boron-doped carbon powders formed at 1000 C and one atmosphere, Carbon, 46 (2008) 1711-1717. https://doi.org/10.1016/j.carbon.2008.07.022

54. E. Mele, J. Ritsko, Electronic excitations in boron-doped graphite, Phy. Rev. B, **24**, (1981) 1000. https://doi.org/10.1103/PhysRevB.24.1000

55. L. Yang, S. Jiang, Y. Zhao, L. Zhu, S. Chen, X. Wang, Q. Wu, J. Ma, Y. Ma, Z. Hu, Boron-doped carbon nanotubes as metal-free electrocatalysts for the oxygen reduction reaction. Ang. Chem. 123 (2011) 7270-7273. https://doi.org/10.1002/anie.201101287

56. D. Buttry, A. Bard, Electroanalytical chemistry, vol. 17. New York: Marcel Dekker (1991).

57. P. Zuman, R.N. Adams, Electrochemistry at solid electrodes: M. Dekker, New York, 1969, xiii+ 402 pp. Elsevier 1970 (1970).

58. A. Anithaa, K. Asokan, C. Sekar, Swift heavy nickel ion irradiated ethylene diamine tetra acetic acid-assisted tungsten trioxide thin film for the electrocatalytic detection of guanine, Sens. Actuators B, 247 (2017) 814-822. https://doi.org/10.1016/j.snb.2017.03.109

59. M. Arvand, M. Sanayeei, S. Hemmati, Label-free electrochemical DNA biosensor for guanine and adenine by ds-DNA/poly (L-cysteine)/Fe3O4 nanoparticles-graphene oxide nanocomposite modified electrode, Biosens. Bioelectron. 102 (2018) 70-79. https://doi.org/10.1016/j.bios.2017.11.002

60. N. Akhtar, S.A. El-Safty, M.E. Abdelsalam, H. Kawarada, One-pot fabrication of dendritic NiO@ carbon–nitrogen dot electrodes for screening blood glucose level in diabetes, Adv. Healthcare Mater. 4 (2015) 2110-2119. https://doi.org/10.1002/adhm.201500369

61. A.A. Abdelwahab, A.H. Naggar, M. Abdelmotaleb, M.Y. Emran, Ruthenium nanoparticles uniformly-designed chemically treated graphene oxide nanosheets for simultaneous voltammetric determination of dopamine and acetaminophen. Electroanalysis, (2020). https://doi.org/10.1002/elan.202060126

62. R. Rahbari, T. Sheahan, V. Modes, P. Collier, C. Macfarlane, R.M. Badge, A novel L1 retrotransposon marker for HeLa cell line identification. Biotechniques, 46 (2009) 277. https://doi.org/10.2144/000113089

63. J.N. Davidson, The biochemistry of the nucleic acids: Elsevier 2012.

64. P. Wang, H. Wu, Z. Dai, X. Zou, Simultaneous detection of guanine, adenine, thymine and cytosine at choline monolayer supported multiwalled carbon nanotubes film, Biosens. Bioelectron. 26 (2011) 3339-3345. https://doi.org/10.1016/j.bios.2011.01.011

65. X. Li, M.A. Shenashen, X. Wang, A. Ito, A. Taniguchi, S.A. El-Safty, Hierarchically porous, and Cu-and Zn-containing γ-AlOOH mesostrands as adjuvants for cancer immunotherapy, Sci. Rep. 7 (2017) 16749. https://doi.org/10.1038/s41598-017-12446-9

66. X. Li, M.A. Shenashen, X. Wang, A. Ito, A. Taniguchi, S.A. El-Safty, Mesoporous Caged-γ-AlOOH-Double-Stranded RNA Analog Complexes for Cancer Immunotherapy, Adv. Biosystems, 2 (2018) 1700114. https://doi.org/10.1002/adbi.201700114

Figures caption

Scheme 1. A) The designed electrode of NMS shows multifunctional centers of B-atoms doped the carbon chain, heterogenous surface of various geomatics of ridges end, rugged surface texture, and grooves. B) The living cells exposed oxidative stresses and the cell's function may have changed as the cell's DNA damage. C) The DNA in the cell's nucleus damaged as exposed to the oxidative stresses such as the OH• which leads to the releasing of the DNA-nucleobases of Ad, Gu, cytosine, and Th.

Figure 1. A) FE-SEM images of NMS-2 with a) low magnification, and b&c) high magnification. B) WA-XRD of NMS-1 (blue line), and NMS-2 (wine line). C) Raman shift spectra of NMS-1 (blue line), and NMS-2 (wine line). N_2-adsorption-desorption isotherm of NMS-1 (D), and NMS-2 (E) materials were obtained. BJH pore size distribution of NMS-1 (inset of D), and NMS-2 (inset of E). F) HR-TEM-image of NMS-2 with low magnification (a), high magnification (b). G) DF-EDS-STEM-mapping of NMS-2 for obtaining the atomic distribution of C (b), O (c), and B (d).

Figure 2. A) Cyclic voltammograms (CVs) of GCE (black line), NMS-1 (blue line), and NMS-2 (wine line) in 0.1 M KCl containing 1 mM $K_3[Fe(CN)_6]$ at a scan rate of 100 mVs^{-1}. B and its inset) EIS of GCE (black line), NMS-1 (blue line), and NMS-2 (wine line) in 0.1 M KCl containing 1 mM $K_3[Fe(CN)_6]$. CVs of 20 µM Gu (C), 10 µM Ad (D), and 10 µM Th (E) in 0.1 M PBS (pH = 7) at a scan rate of 0.1 Vs^{-1} on GCE (black line), NMS-1 (blue line), and NMS-2 (wine line). F) CVs of simultaneous detection of 10 µM Gu +20 µM Ad +10 µM Th in 0.1 M PBS (pH = 7) at a scan rate of 0.1 Vs^{-1} on GCE (black line), NMS-1 (blue line), and NMS-2 (wine line).

Figure 3. CVs of pH-dependent monitoring assay of 10 µM Gu (A), and 10 µM Ad (C) within varying the pH range of 6-9 at scan rate 100 mVs^{-1}, and at room temperature on the NMS-2. (E) CVs of the various pH various from 6 -7.4 for 50 µM Th at scan rate 100 mVs^{-1}, and at room temperature on NMS-2. Plots of the pH values versus the anodic current (µA) and applied potential E (V) for Gu (B), Ad (D), and Th (F) using NMS-2. G) CVs of 40 µM Gu at varying scan rate (0.05-0.25 Vs^{-1}) in 0.1 M PBS (pH = 7.4) on the NMS-2, and J) Plot of scan rate (mVs^{-1}) vs the corresponding anodic currents (µA). H) CVs of 20 µM Ad at varying scan rate (0.05-0.25 Vs^{-1}) in 0.1 M PBS (pH =7.4) on the NMS-2, and K) plot of the square rote of scan rate (mVs^{-1}) vs the corresponding anodic currents (µA). I) CVs of 100 µM Th at varying scan rate (0.05-0.25 Vs^{-1}) in 0.1 M PBS (pH = 7.4) on the NMS-2, and L) plot of scan rate (mVs^{-1}) vs the corresponding anodic currents (µA).

Figure 4. A) Individual detection of Gu (a) using SWV- measurements of NMS-2 at varying Gu concentrations (0.01-1 µM) in the presence of 0.04 µM Ad, and 40 µM Th, varying the Ad-concentrations (b) ranged from 0.04 µM - 0.8 µM in the presence of 0.1 µM

Gu, and 40 µM Th, and varying Th-concentrations (c) ranged from 0.05 µM - 0.5 µM in the presence of 0.1 µM Gu, and 0.1 µM Ad. (B) Calibration plot of [Gu]/ µM (a), [Ad]/ µM (b), and [Th]/ µM (c) vs the currents (µA). The insets of a, and b are the calibration plot at low concentrations of Gu, and Ad, respectively. (C) SWV-measurements of one step adding of Gu (0.25-3 µM), Ad (0.25 - 3 µM), and Th (0.5-10 µM) in 0.1 M PBS (pH = 7.4) at step amplitude = 15 mV, frequency = 20 Hz, time of integration = 3 ms and step height = 0.3 mV. Inset of C) Calibration plot of one step adding of Gu, and Ad, and Th - concentrations (µM) vs the currents (µA). D) Amperometry response of various concentrations of Gu at 0.8 V (black line), Ad at 1.1 V (red line), and Th at 1.3 V (violet line).

Figure 5. A-D) Confocal microscopy images recorded at an excitation wavelength of 488 nm and emission wavelength at 620 nm of control cells (Hela cells). A) Bright-field image of NMS-2 incubated with Hela cells. B) Nucleus blue staining (DAPI) of Hela cells image. C) F- actine (phalloidin)photo image of the Hela cells. D) Merged image for Hela cells upon incubation with NMS-2. The Dot plots of the flow cytometry obtained for Hela cells (5×10^5) as control (E), and Hela cells (5×10^5) incubated with 40 µg/mL NMS-2 for 30 min (F). G) SWV-measurement of the supernatants of Hela cells medium ($5x10^4$ cells/ mL) after incubation with Fenton reagent for 4 h, which detecting the DNA-nucleobases on NMS-2. H) SWV-measurement of the supernatants of A549 cell medium ($5x10^4$ cells mL^{-1}) after incubation with Fenton reagent for 4 h, which detecting the DNA-nucleobases on NMS-2.

Figure 6. The column plot of the number of samples and electrodes for providing the stability, and reproducibility of Gu (A&D), Ad (B&E), and Th (C&F) on NMS-2 using SWV-measurements in 0.1 PBS (pH = 7.4). The NMS-2 stability of 0.5 µM Gu (G), 0.5 µM Ad (H), and 0.5 µM Th (I) for a prolonged time was studied and measured by SWV.

Scheme 1

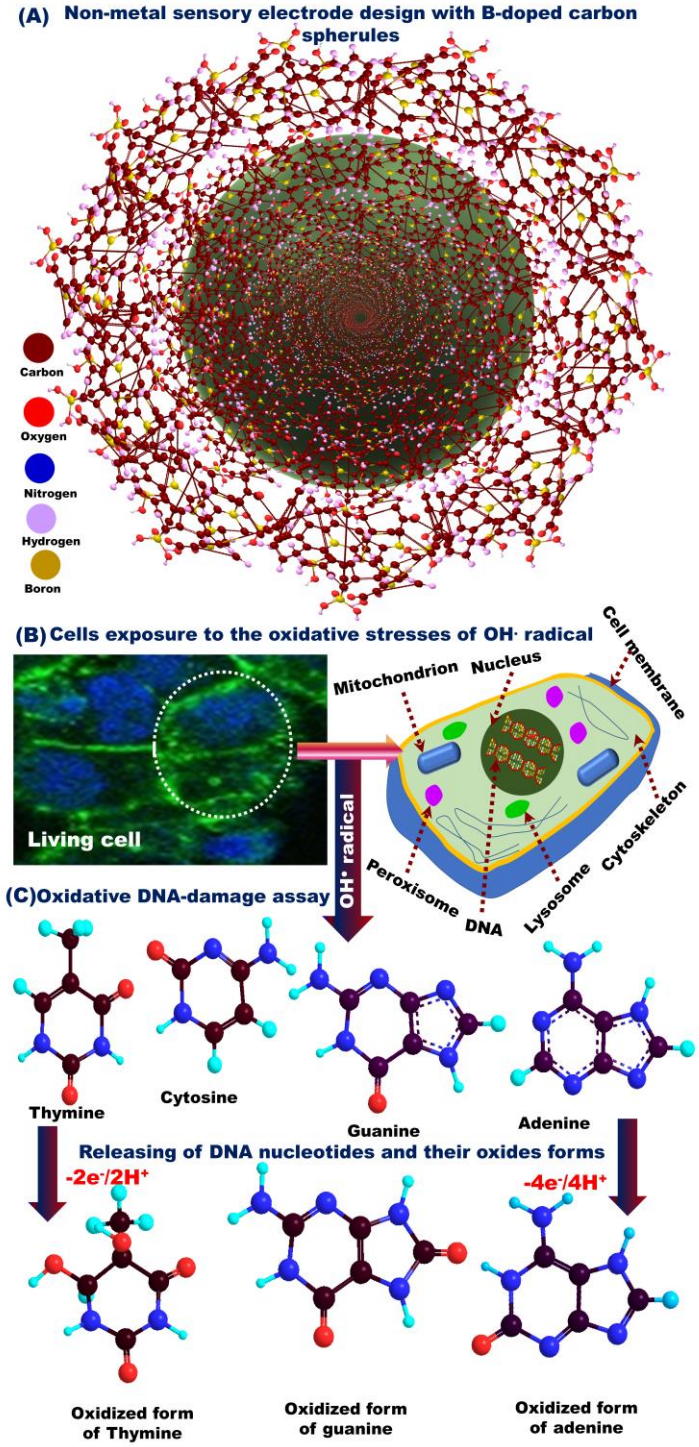
(A) Non-metal sensory electrode design with B-doped carbon spherules
Carbon
Oxygen
Nitrogen
Hydrogen
Boron
(B) Cells exposure to the oxidative stresses of OH· radical
Living cell
OH· radical
Mitochondrion
Nucleus
Cell membrane
Peroxisome
DNA
Lysosome
Cytoskeleton
(C)Oxidative DNA-damage assay
Thymine
Cytosine
Guanine
Adenine
Releasing of DNA nucleotides and their oxides forms
-2e⁻/2H⁺
-4e⁻/4H⁺
Oxidized form of Thymine
Oxidized form of guanine
Oxidized form of adenine

Figure 1

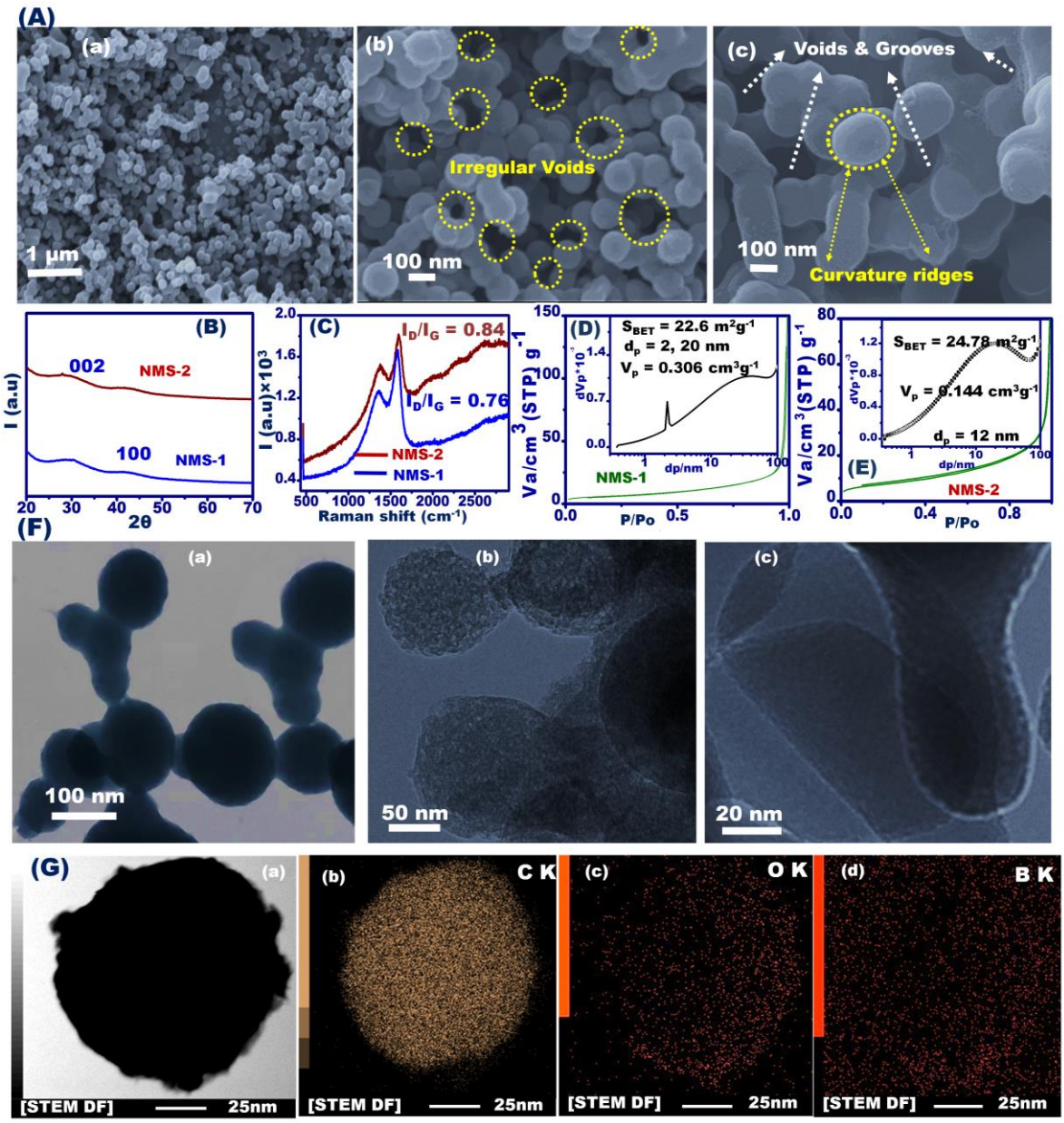
(A)
(a)
1 μm
(b)
Irregular Voids
100 nm
(c)
Voids & Grooves
100 nm
Curvature ridges
(B)
002
NMS-2
100
NMS-1
I (a.u)
2θ
(C)
I_D/I_G = 0.84
I_D/I_G = 0.76
NMS-2
NMS-1
I (a.u)×10³
Raman shift (cm⁻¹)
(D)
S_{BET} = 22.6 m²g⁻¹
d_p = 2, 20 nm
V_p = 0.306 cm³g⁻¹
NMS-1
dp/nm
Va/cm³(STP) g⁻¹
P/Po
(E)
S_{BET} = 24.78 m²g⁻¹
V_p = 0.144 cm³g⁻¹
d_p = 12 nm
dp/nm
NMS-2
P/Po
(F)
(a)
100 nm
(b)
50 nm
(c)
20 nm
(G)
(a)
[STEM DF]
25nm
(b)
C K
[STEM DF]
25nm
(c)
O K
[STEM DF]
25nm
(d)
B K
[STEM DF]
25nm

Figure 2

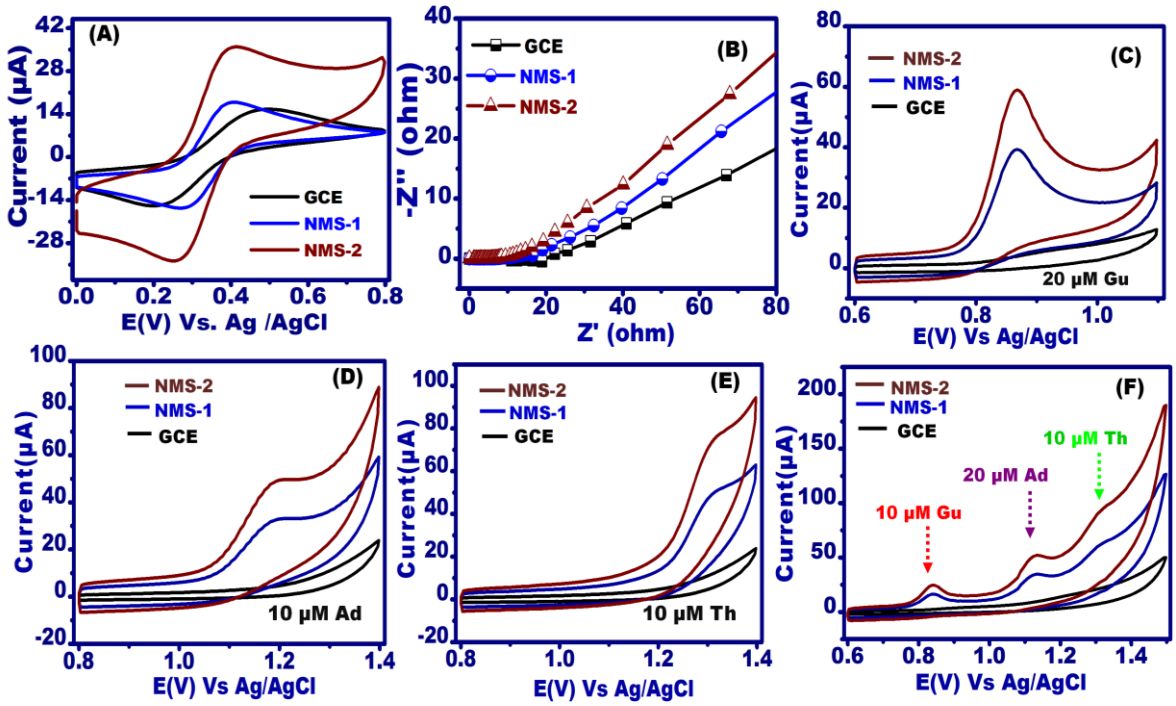
(A)
Current (μA)
E(V) Vs. Ag /AgCl
GCE
NMS-1
NMS-2
(B)
-Z'' (ohm)
Z' (ohm)
GCE
NMS-1
NMS-2
(C)
Current(μA)
E(V) Vs Ag/AgCl
NMS-2
NMS-1
GCE
20 μM Gu
(D)
Current(μA)
E(V) Vs Ag/AgCl
NMS-2
NMS-1
GCE
10 μM Ad
(E)
Current(μA)
E(V) Vs Ag/AgCl
NMS-2
NMS-1
GCE
10 μM Th
(F)
Current(μA)
E(V) Vs Ag/AgCl
NMS-2
NMS-1
GCE
10 μM Th
20 μM Ad
10 μM Gu

Figure 3

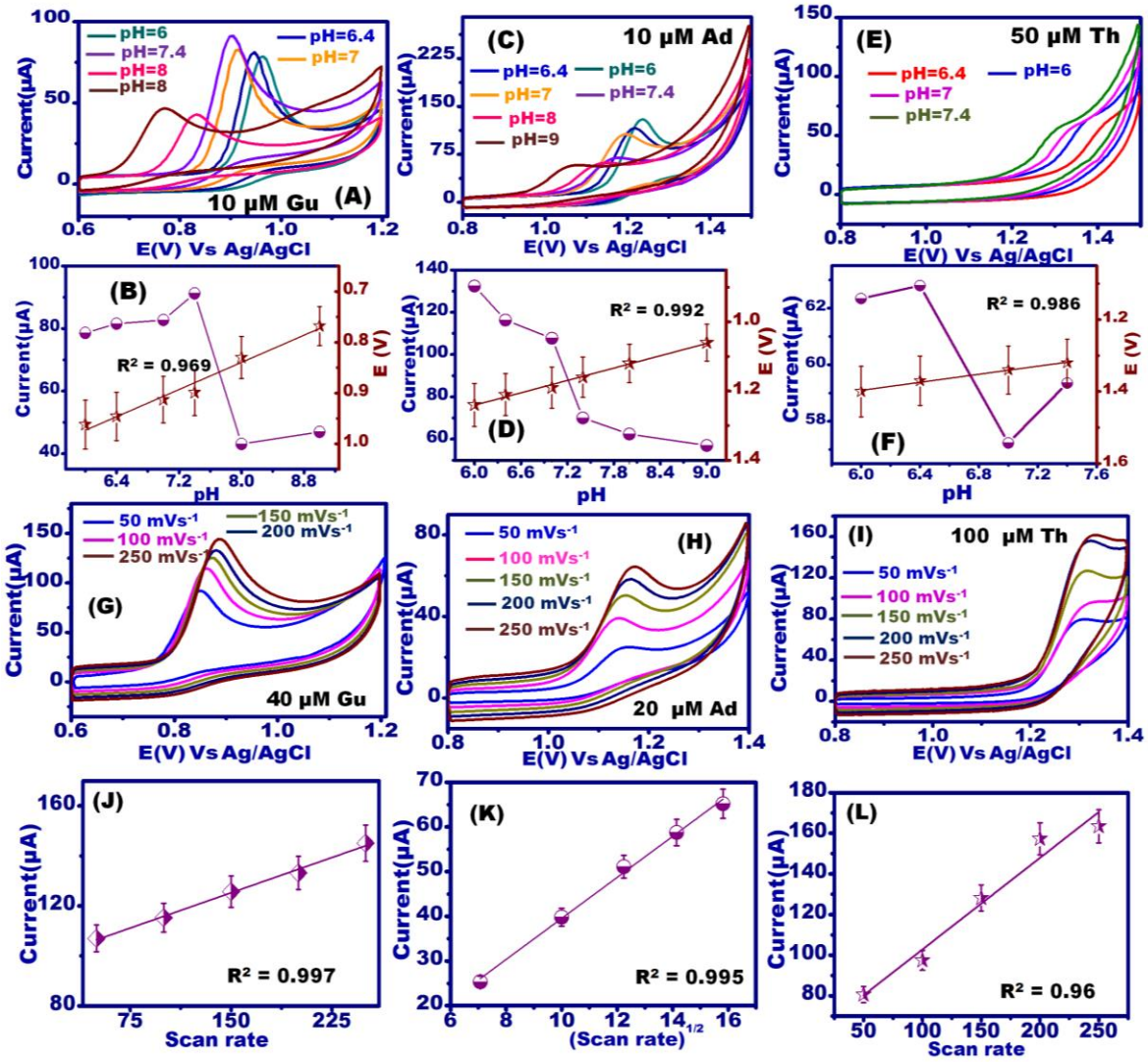
(A)
10 µM Gu
pH=6
pH=7.4
pH=8
pH=8
pH=6.4
pH=7
Current(µA)
E(V) Vs Ag/AgCl
(C)
10 µM Ad
pH=6.4
pH=6
pH=7
pH=7.4
pH=8
pH=9
(E)
50 µM Th
pH=6.4
pH=6
pH=7
pH=7.4
(B)
R² = 0.969
E (V)
pH
(D)
R² = 0.992
(F)
R² = 0.986
(G)
50 mVs-1
100 mVs-1
150 mVs-1
200 mVs-1
250 mVs-1
40 µM Gu
(H)
20 µM Ad
(I)
100 µM Th
(J)
R² = 0.997
Scan rate
(K)
R² = 0.995
(Scan rate)1/2
(L)
R² = 0.96
Scan rate

Figure 4

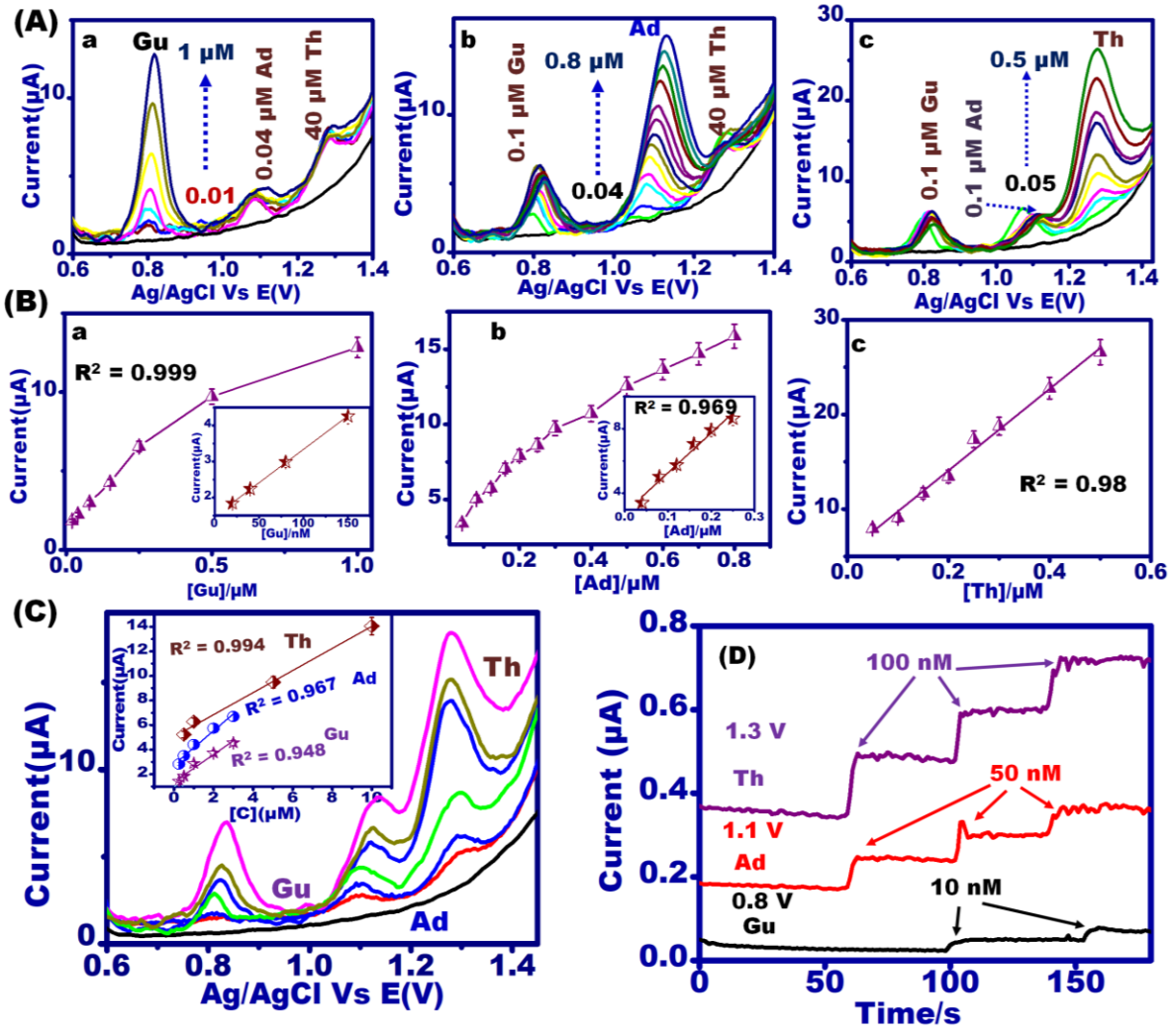
(A)
a
Gu
1 μM
0.01
0.04 μM Ad
40 μM Th
b
0.1 μM Gu
0.8 μM
0.04
Ad
40 μM Th
c
0.1 μM Gu
0.1 μM Ad
0.5 μM
0.05
Th
Current(μA)
Ag/AgCl Vs E(V)
(B)
a
R² = 0.999
[Gu]/μM
[Gu]/nM
b
R² = 0.969
[Ad]/μM
c
R² = 0.98
[Th]/μM
(C)
R² = 0.994 Th
R² = 0.967 Ad
R² = 0.948 Gu
[C](μM)
Th
Gu
Ad
(D)
100 nM
1.3 V
Th
50 nM
1.1 V
Ad
10 nM
0.8 V
Gu
Current (μA)
Time/s

Figure 5

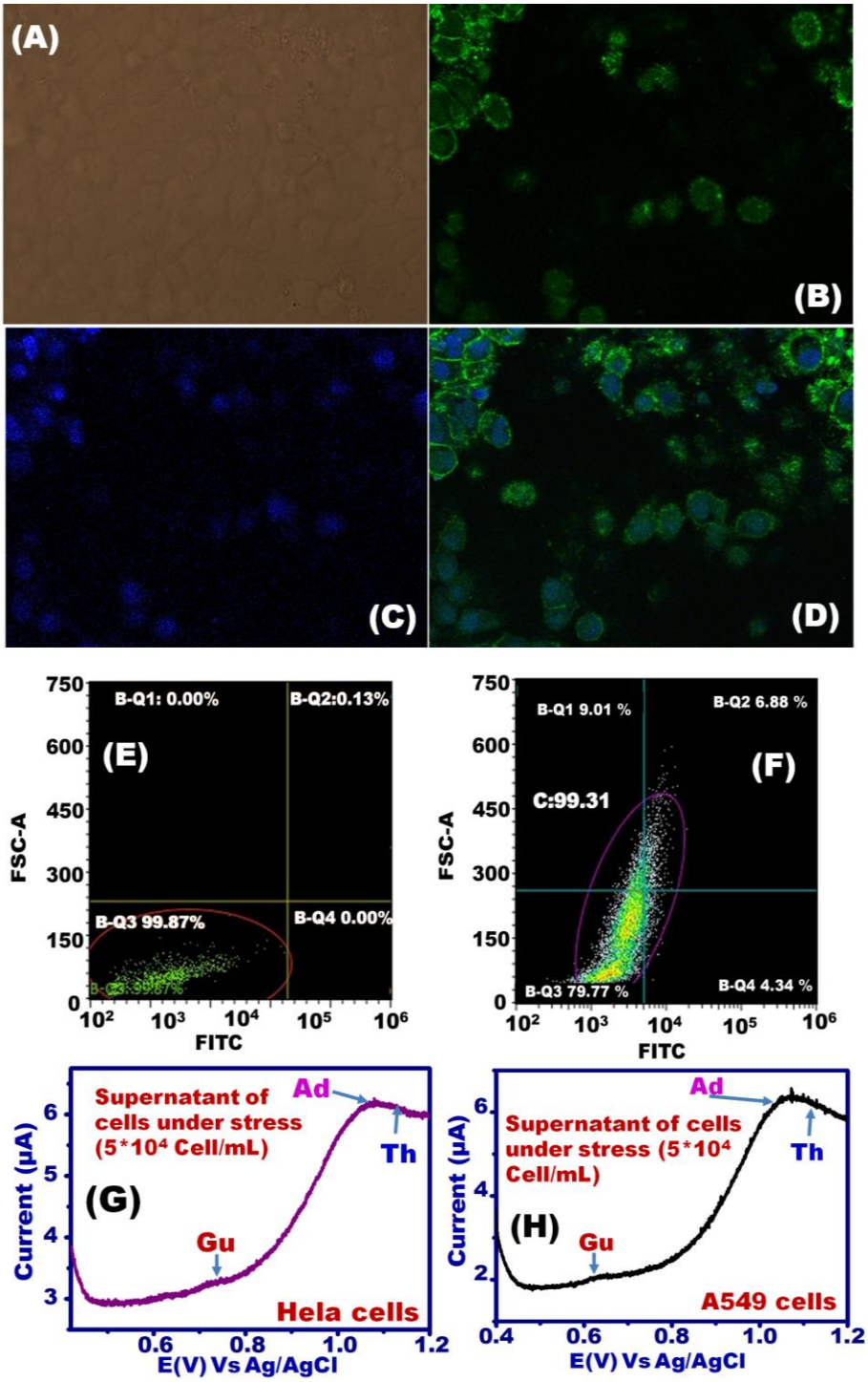
(A)
(B)
(C)
(D)
(E)
B-Q1: 0.00%
B-Q2:0.13%
B-Q3 99.87%
B-Q4 0.00%
FSC-A
FITC
(F)
B-Q1 9.01 %
B-Q2 6.88 %
C:99.31
B-Q3 79.77 %
B-Q4 4.34 %
Supernatant of cells under stress (5*10⁴ Cell/mL)
Ad
Th
Gu
(G)
Hela cells
Current (μA)
E(V) Vs Ag/AgCl
(H)
A549 cells

Figure 6

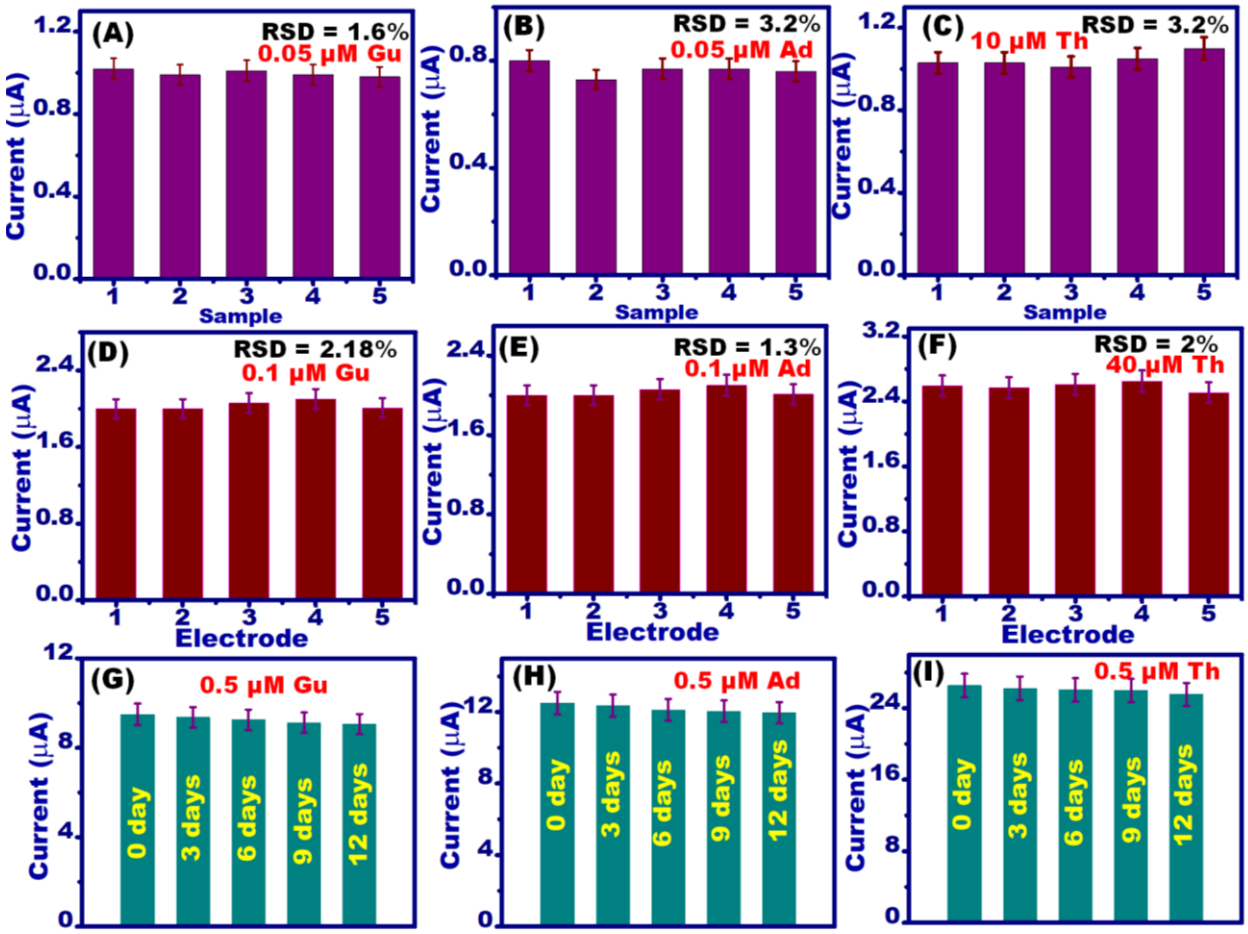
(A)
RSD = 1.6%
0.05 μM Gu
(B)
RSD = 3.2%
0.05 μM Ad
(C)
10 μM Th
RSD = 3.2%
(D)
RSD = 2.18%
0.1 μM Gu
(E)
RSD = 1.3%
0.1 μM Ad
(F)
RSD = 2%
40 μM Th
(G)
0.5 μM Gu
(H)
0.5 μM Ad
(I)
0.5 μM Th
Current (μA)
Sample
Electrode
0 day
3 days
6 days
9 days
12 days